analytical chemistry

pubs.acs.org/ac Article

Photoswitchable Machine-Engineered Plasmonic Nanosystem with High Optical Response for Ultrasensitive Detection of microRNAs and Proteins Adaptively

Sumon Hati,[⊥] Sarah R. Langlais,[⊥] Adrianna N. Masterson, Thakshila Liyanage, Barry B. Muhoberac, Hristos Kaimakliotis, Merrell Johnson, and Rajesh Sardar*

Cite This: *Anal. Chem.* 2021, 93, 13935−13944 Read Online

ACCESS | Metrics & More | Article Recommendations | Supporting Information

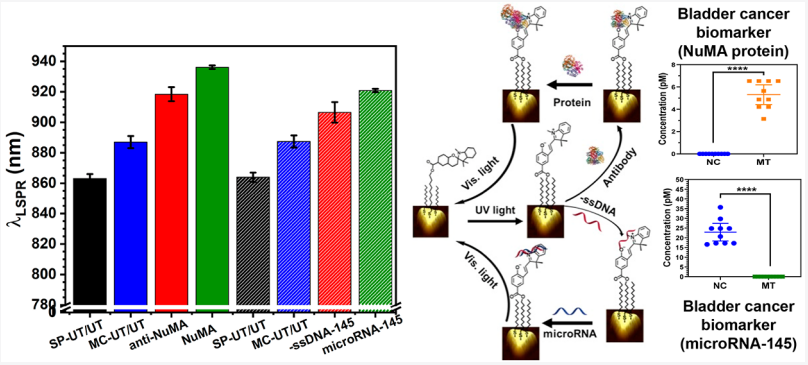

ABSTRACT: Modulating optoelectronic properties of inorganic nanostructures tethered with light-responsive molecular switches by their conformational change in the solid state is fundamentally important for advanced nanoscale-device fabrication, specifically in biosensing applications. Herein, we present an entirely new solid-state design approach employing the light-induced reversible conformational change of spiropyran (SP)-merocyanine (MC) covalently attached to gold triangular nanoprisms (Au TNPs) via alkylthiolate self-assembled monolayers to produce a large localized surface plasmon resonance response (∼24 nm). This shift is consistent with the increase in thickness of the local dielectric shell-surrounded TNPs and perhaps short-range dipole−dipole (permanent and induced) interactions between TNPs and the zwitterionic MC form. Water contact angle measurement and Raman spectroscopy characterization unequivocally prove the formation of a stable TNP-MC structural motif. Utilizing this form, we fabricated the first adaptable nanoplasmonic biosensor, which uses an identical structural motif for ultrasensitive, highly specific, and programmable detection of microRNAs and proteins at attomolar concentrations in standard human plasma and urine samples, and at femtomolar concentrations from bladder cancer patient plasma (n = 10) and urine (n = 10), respectively. Most importantly, the TNP-MC structural motif displays a strong binding affinity with receptor molecules (i.e., single-stranded DNA and antibody) producing a highly stable biosensor. Taken together, the TNP-MC structural motif represents a multifunctional super biosensor with the potential to expand clinical diagnostics through simplifying biosensor design and providing highly accurate disease diagnosis.

INTRODUCTION

Reversible manipulation of interfacial properties of nanoscale objects with external stimuli (e.g., light, heat, magnetic field) is of the utmost importance for applications in the fields of chemistry, biology, and medicine.[1−9] Among many photoswitchable molecules (azobenzene, rotaxane, stilbenes, and fulgides), the photoisomerization of spiropyran (SP, molecular switch) has been studied both for fundamental purposes and potential applications in sensing, imaging, and drug delivery.[10−12] Light-induced isomerization of such a "molecular switch" in the solid-state provides several investigative advantages: (1) fast response and no leaching, (2) nondestructive cycling and reduced photodegradation, (3) high precision of its structural conformation, and (4) on demand tuning and modulation of electronic properties and functions. Irradiation of SP by UV light (<400 nm) opens the oxygen-containing ring, leading to the formation of merocyanine (MC), whereas exposure to visible light (>450 nm) causes the reverse transition. In the literature, we find that the surface of inorganic nanostructures can be modified with SP-containing SAMs to

Received: July 15, 2021
Accepted: September 10, 2021
Published: October 4, 2021

https://doi.org/10.1021/acs.analchem.1c02990
Anal. Chem. 2021, 93, 13935−13944

modulate their localized surface plasmon resonance (LSPR) response via a self-assembly process in solution. Also, such a solution phase functionalization of quantum dots influences their fluorescence properties due to alteration in energy transfer.[13] Previously, chemically tethered SP/MC attached to a solid surface was studied for fundamental purposes[14−16] and biosensing application.[17] In this context, observation of light-induced photoisomerization of molecular switches chemically tethered onto plasmonic nanostructures by monitoring their LSPR properties in the solid state is rare.[18−20] To the best of our knowledge, no report is available that demonstrates the optical response of metallic nanostructures (mainly LSPR properties) together with nanoplasmonic biosensor development utilizing SP-to-MC photoisomerization in the solid state.

Design of an appropriately constructed SP—self-assembled monolayer (SAM)—modified plasmonic nanostructure that is a photoswitchable solid-state molecular device in which light induced changes in structural and electronic properties of the organic moiety may influence electronic properties, can be studied by monitoring LSPR responses. Such properties of metallic nanostructures depend not only on size, shape, and local dielectric environment but also short-range, interparticle coupling.[21,22] Therefore, an appropriate nanostructure−SAM−SP/MC construct in a well-defined physicochemical environment has the unique potential for the development of highly efficient sensors. In this article, we report a dramatic change in LSPR properties of gold triangular nanoprisms (Au TNPs) functionalized with SAMs of alkylthiols containing covalently bound SP during their solid-state photoisomerization. An unprecedentedly large shift of the TNP dipole peak ($\Delta\lambda_{LSPR}$) is observed during photoisomerization between SP and MC forms. We used a suite of spectroscopic techniques along with density functional theory (DFT) calculations to investigate the highly reproducible photoisomerization of SP/MC in the solid-state.

Finally, starting with the MC form, we designed and fabricated an LSPR-based, adaptable nanoplasmonic biosensor that is capable of ultrasensitive detection of microRNAs (microRNA-10b, and -145) and proteins (nuclear mitotic apparatus protein-1, NuMA) from cancer patient biofluids (plasma and urine) with high specificity. Importantly, these cancer biomarkers were detected with an identical biosensor construct by programmable exchange of -ssDNA or protein receptor molecules that electrostatically adsorbed onto the activated MC form and detected either the microRNA or the protein. We believe that this work presents a significant advancement in the field of biosensing because modern univariant "*gold standard*" bioanalytical techniques (RT-PCR, microarray, sequencing, ELISA, etc.) almost exclusively operate in a discrete format unable to assay different types of biomolecules using a single instrument. For example, RT-PCR is capable of assaying nucleic acids but not proteins, whereas ELISA only assays proteins but not RNAs. In contrast, the TNP-SAM-SP/MC construct would allow the detection of any biomarkers by utilizing specific receptor molecules without altering the biosensor's basic structural motifs, workflow, and readout instruments. Taken together, in this study, we introduce a novel nanosystem that could simplify biosensor design and improve outcomes for clinical cancer diagnostics.

EXPERIMENTAL SECTION

Materials. 3-Mercaptopropyl-trimethoxysilane (MPTMS, 94%) and 1-nonanethiol (98%) were purchased from Alfa Aesar. Ethanol (EtOH; 200 proof) was purchased from Decon Laboratories. Chloro(triethylphosphine) gold(I) (Et_3PAuCl, 97%) was purchased from Gelest Inc. Poly-(methylhydrosiloxane) (PMHS, M_n = 1700−3300), triethylamine (TEA, 98%), hexamethylene tetramine (HMTA, ≥99.0%), 1,3,3-trimethyl-2-methylene indoline (TMMI, 97%), dimethyl aminopyridine (DMAP, ≥ 98.0%), 11-mercaptoundecanol (97%), 1-undecanethiol (UT, 98%), 1-hexanedecanethiol (≥95.0%), 1-hexanethiol (98%), and ACS grade acetonitrile (CH_3CN, 99.9%) were purchased from Sigma-Aldrich. All nucleic acid oligos, single stranded oligonucleotide-145 (-ssDNA-145) and single stranded oligonucleotide-10b (-ssDNA-10b), nucleic acid RNAs, single stranded microRNA-145 (microRNA-145), and single stranded microRNA-10b (microRNA-10b), were purchased from Integrated DNA Technologies (IDT). NuMA protein (NuMA) was purchased from Sigma Prestige, and Antiphoso-NuMA-1 (Anti-NuMA) was purchased from EMD Millipore Corporation. 1-Octadecanethiol (≥95.0%) was purchased from Fluka Analytical. Baxter Healthcare Corporation provided RNase free sterile water. RBS 35 Detergent, 25 × 25 mm glass coverslips, trifluoroacetic acid (TFA, 99%), and dichloromethane (DCM) were purchased from Fisher Scientific. 4-Hydroxy benzoic acid (BA, 99%) and N,N-dicyclohexylcarbdiimide (99%) were purchased from Acros Organics. Methanol (MeOH) and ethyl acetate (EtOAc) were purchased from Pharmco. All water was purified using a Thermo Scientific Barnstead Nanopure system. Thiol modified nucleic acid oligos (-ssDNAs), microRNAs, antibodies, proteins, and patient samples were stored at −80 °C. PBS buffer (pH = 7.2) was prepared using the above-mentioned RNase free sterile water.

Spiropyran (SP)-Functionalized Au TNP Nanoplasmonic Biosensors. Following SP-COO-$(CH_2)_{11}$-SH synthesis, Au TNP-functionalized glass coverslips cut into 1 cm width pieces, were incubated in a mixture of 75:25 SP-UT (0.025M):UT (0.025M) overnight. The formation of a mixed self-assembled monolayer (SAM) of SP-UT:UT was confirmed by measuring the LSPR dipole peak position (λ_{LSPR}) of Au TNPs. Utilizing the photochromic nature of SP, coverslips were then irradiated with 360 nm UV light for 10 min forcing the closed-ring SP structure into the open-ring zwitterionic MC form. The λ_{LSPR} was used to confirm the photoisomerization. Once in the activated MC form, the now fully functional zwitterionic biosensor was then utilized to bind a target receptor (-ssDNA-145 or -ssDNA-10b) or antibody (Anti-NuMA) and the analyte (microRNA-145, microRNA-10b or NuMA) as described below.

Biosensor Reversibility and Regeneration. The SP/MC functionalized biosensors described above have the ability to be regenerated to detect biomarkers without a change in specificity or sensitivity. This was accomplished by taking the biomarker attached coverslips, either -ssDNA/microRNA or antibody/protein, washed with PBS buffer and irradiating it with visible light at 450 nm for 10 min. This facilitated the open-ring, MC form to photoisomerize back into the original closed-ring SP form thereby releasing all bound receptors and/or analytes. Once the inactivated SP biosensor is regenerated, the above procedure for the zwitterionic MC form is repeated with reattachment of the same or different receptor/analyte pair. This process can be repeated without altering the sensitivity or specificity of the sensing platform.

Analyte Quantification of microRNA (microRNA-145 and -10b) and Protein (NuMA) in Bladder Cancer Patient

https://doi.org/10.1021/acs.analchem.1c02990
Anal. Chem. 2021, 93, 13935−13944

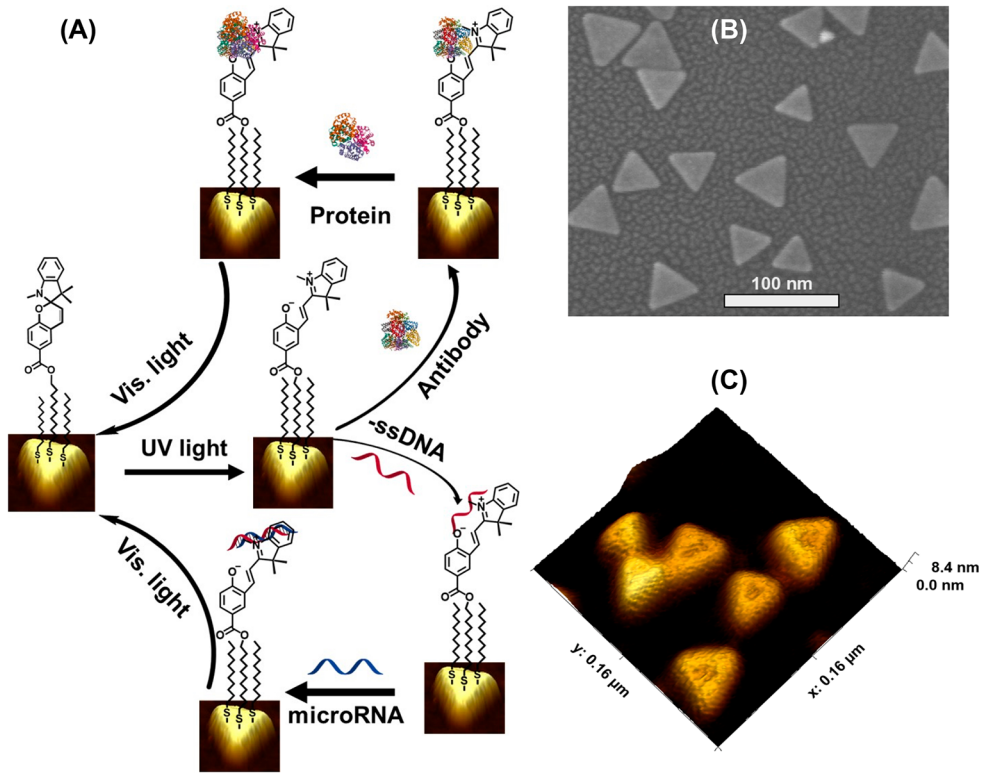

Figure 1. Adaptable, nanoplasmonic biosensor construction and structural characterizations. (A) Schematic illustration of functionalized Au TNPs as a multimodal molecular sensor and biosensor for the detection of microRNAs and proteins. Au TNPs were attached onto a thiolated silane-functionalized glass coverslip, and the TNP surface was modified with a 75%:25% ratio of SP-UT and UT SAMs to fabricate a molecular sensor (a). Then the coverslip was exposed to UV light to create the MC-UT form (b). The coverslips were incubated in PBS buffer containing either -ssDNA or receptor protein. (c) -ssDNAs or (d) protein electrostatically adsorbed onto zwitterionic MC surface that makes our "nanoplasmonic biosensor". The biosensor was incubated overnight in either human plasma or urine supplemented with microRNA or protein. Here, -ssDNA (receptor) has the complementary base pair for the target microRNA (analyte) (e), and receptor protein specifically binds to analyte protein (f). Receptor molecules and bound analytes are dissociated by light exposure, and new receptors and analytes can bind completing the cycle and making the biosensor adaptable. Representative scanning electron (B) and atomic force (C) microscopy images of Au TNPs.

Plasma and urine. For patient plasma samples, biosensors were incubated in a solution containing 100 μL of metastatic patient plasma (or normal control—cancer negative patient plasma) diluted to a total of 6 mL of PBS buffer for 24 h and then were thoroughly washed with PBS buffer to remove any nonspecifically adsorbed biomolecules, and the λ_{LSPR} was recorded. The $\Delta\lambda_{LSPR}$ was determined for each patient, and the concentration of microRNA was quantified utilizing the developed corresponding biomarker calibration curve. For patient urine samples, biosensors were incubated in a solution containing 500 μL of metastatic patient urine (or normal control - cancer negative patient urine) diluted with 4.5 mL of RNase free water for 24 h and then were thoroughly washed with RNase free water to remove any nonspecifically adsorbed biomolecules, and the λ_{LSPR} was recorded. The $\Delta\lambda_{LSPR}$ was determined for each patient, and the concentration of protein was quantified utilizing the developed corresponding biomarker calibration curve.

RESULTS AND DISCUSSION

Fabrication and Characterization of the Photoswitching Molecular Device. To construct our plasmonic-based molecular device consisting of molecular switches (machines), we functionalized Au TNPs attached to a silanized glass coverslip with an SP-linked undecanethiol (SP-UT) SAM, with the result shown schematically in Figure 1A. We selected Au TNPs due to their excellent photostability and large LSPR response that originates from high electromagnetic (EM) field enhancement at the sharp tips and corners.[23,24] We and others have shown that Au TNPs are a unique type of nanostructure for highly sensitive molecular and biological sensor construction.[18,25−29] We started with triethylamine (TEA)-passivated TNPs with an average 42 nm edge length and ∼8 nm height (Figure 1B,C) that display λ_{LSPR} at 800 nm in the air (see Figure 2A). The average density of Au TNPs onto the surface is 180/μm^2. Ligand exchange of these TNPs with a 0.025 M acetonitrile solution of SP-UT (100%) results in a $\Delta\lambda_{LSPR}$ of 68 ± 11 nm in air. This large shift could potentially result exclusively from the change in the thickness of a local dielectric shell originating from the hydrocarbon SAM around the TNPs versus TEA. In contrast, a much smaller $\Delta\lambda_{LSPR}$ of 28 ± 7 nm is observed when TNPs were functionalized with only undecancethiol (UT, without SP) SAMs. We modeled (ChemDraw 3D) a fully extended UT and SP-UT and found a theoretical thicknesses of 1.43 and 2.66 nm, respectively. The difference in thickness between UT and SP-UT SAM is ∼1.23 nm and provides an increase in wavelength shift of 40 nm, which is unexpectedly high. To further validate our theoretical argument of the importance of more than just a change in local refractive index, we prepared TNPs with SAMs of different length alkylthiols by varying the methylene unit ($-CH_2$) number to determine the $\Delta\lambda_{LSPR}$ as a function of thickness of the local dielectric shell (Figure S1). These measurements predict that a 2.66-nm-thick

https://doi.org/10.1021/acs.analchem.1c02990
Anal. Chem. 2021, 93, 13935−13944

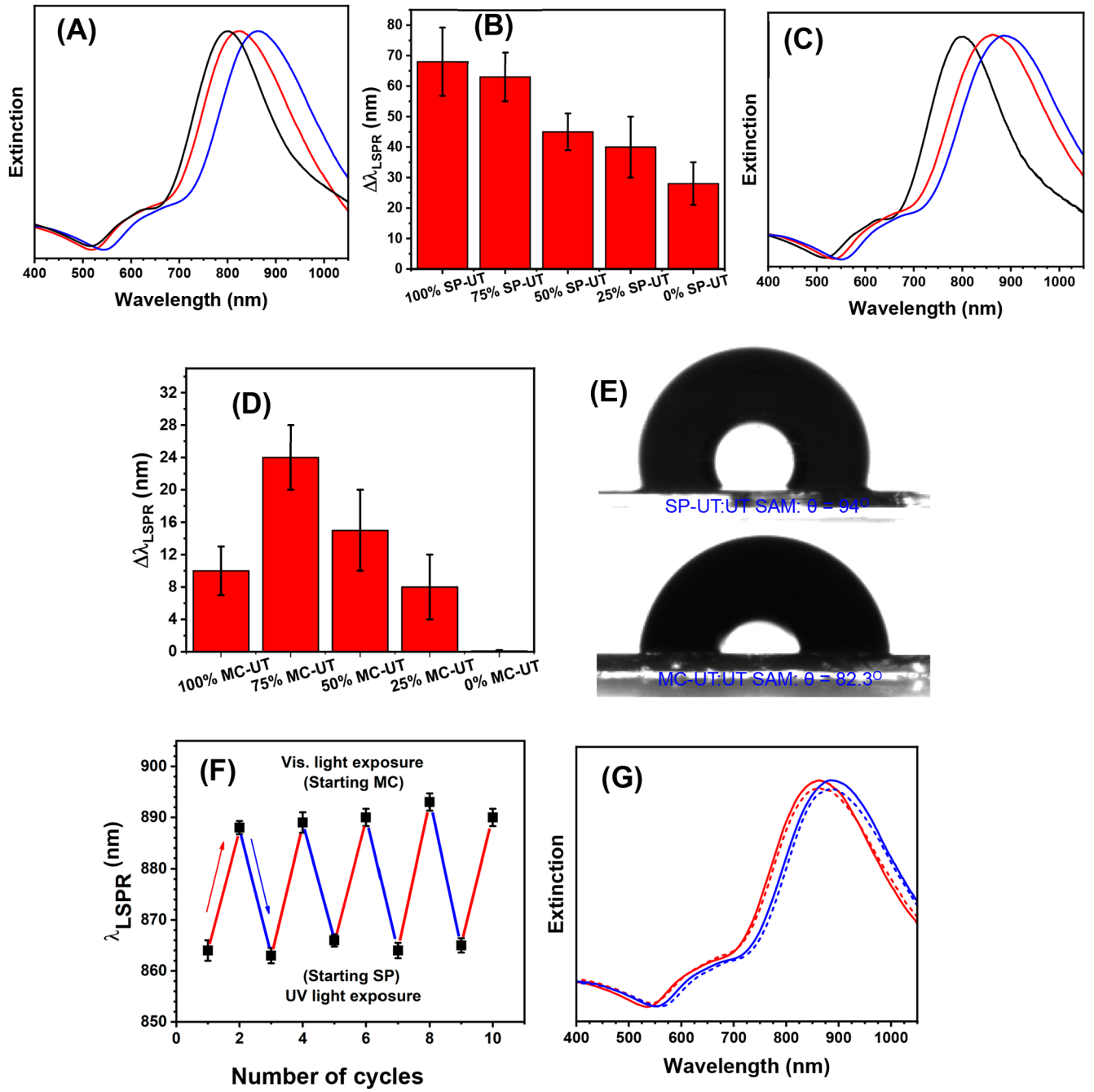

Figure 2. Spectroscopic characterization of the photoisomerizable molecular sensor. (A) UV−visible extinction spectra of Au TNPs before (black, λ_{LSPR} = 800.1 nm), after functionalization with 100% UT (0% SP-UT; red, λ_{LSPR} = 828.1 nm), and with 100% SP-UT (0% UT; blue, λ_{LSPR} = 868.2 nm). (B) Bar graph representation of $\Delta\lambda_{LSPR}$ (nm) for Au TNP functionalization with different percentages of SP-UT (remaining percentage is UT spacer). (C) UV−visible extinction spectra of Au TNPs before (black, λ_{LSPR} = 801.0 nm), after functionalization with 75%:25% SP-UT:UT (SP-UT/UT) SAMs (red, λ_{LSPR} = 864.1 nm), and after exposure to UV light (blue, λ_{LSPR} = 888.3 nm). (D) Bar graph representation of $\Delta\lambda_{LSPR}$ (nm) for transformation of 75%:25% SP-UT to 75%:25% MC-UT form. (E) Water drops on the SP-UT:UT SAM-modified surface (top, θ = 94°) and after UV light irradiation (bottom, θ = 82.3°). (F) The λ_{LSPR} position of the 75%:25% SP-UT:UT SAM-modified nanosystem upon cycling between exposure to UV and visible light. Exposure to UV light caused SP to convert to the MC form, while visible light exposure caused a transition of MC to SP. (G) UV−visible extinction spectra showing reversibility between SP-UT:UT SAM and MC-UT:UT after the first (SP-UT:UT, red, λ_{LSPR} = 864.0 nm and MC-UT:UT, blue, λ_{LSPR} = 888.7 nm) and the fifth (SP-UT:UT, red dashed, λ_{LSPR} = 865.0 nm and MC-UT:UT, blue dashed, λ_{LSPR} = 890.1 nm) cycle. All extinction spectra were collected in the air.

pure alkanethiol dielectric shell would produce a $\Delta\lambda_{LSPR}$ of 55 nm, which is significantly smaller than our experimentally determined value of 68 nm. As shown in Figure 2B, the $\Delta\lambda_{LSPR}$ value decreases monotonically with a lower contribution of SP-UT to the SAMs by varying the mole percentage of SP-UT and UT, suggesting an increasing contribution to the wavelength shift from the structurally complex and longer SP-UT.

One of the main virtues of molecular machines is that they undergo structural isomerization under the influence of external stimuli. Next, we investigated exposure of the SP conformation

https://doi.org/10.1021/acs.analchem.1c02990
Anal. Chem. 2021, 93, 13935−13944

to UV light producing MC and how this affects the bound TNPs. This photoisomerization should influence the molecule-nanostructure interfacial interactions and thus the LSPR property of the adjacent nanostructure. As mentioned above, only a limited study has been conducted to investigate light-induced isomerization of photoresponsive molecules chemically tethered onto plasmonic nanostructures by monitoring their LSPR properties in the solid state.[18−20] Several mixed SAM (varying the mole percentage of SP-UT and UT)-functionalized Au TNPs were exposed to UV light for 10 min in the solid-state, and the λ_{LSPR} position was measured. As illustrated in Figure 2C, conversion of the SP to the MC structure results in a red shift of λ_{LSPR} position. Interestingly, the interaction is not monotonic in percent of SP-UT versus UT, and the highest value ($\Delta\lambda_{LSPR}$ = 24 ± 4 nm) is observed for a 75%:25% mixture of SP-UT and UT SAMs (Figure 2D). In contrast, 100% SP-UT SAMs provide a $\Delta\lambda_{LSPR}$ of 10 nm. We do not fully understand this different LSPR response to mixed SAM composition but believe that the steric hindrance in the solid-state with a 100% SP-UT SAM does not allow all SP molecules to convert to the MC form during light exposure, whereas a lower percentage of SP-UT SAMs would produce a relatively smaller change in the dielectric shell thickness. It has been reported that SP chemically tethered onto a solid substrate requires appropriate assembly control to reduce the steric hindrance in order to observe photoisomerization to MC.[15] In our system, an equal chain length of alkylthiol linker and spacer (11 methylene units) is expected to produce a dense lower layer SAM, whereas the 75%:25% SP-UT:UT mole ratio should allow geometric freedom for SP to undergo structural isomerization above the lower layer SAM under light irradiation. Previously, we demonstrated that an equal chain length of alkylthiol linker and spacer in the SAM is very important for photoisomerization of the molecular machine.[18] Therefore, LSPR results of this work are in agreement with the literature. It is important to mention that a terminal hydroxyl (−OH) group on the alkylthiol spacer could be detrimental to reversible photoisomerization between SP and MC due to proton transfer, as described below. Thus, we used UT as a spacer which has $-CH_3$ terminal group.

To further confirm that conversion to the MC form has caused the observed LSPR peak red shift, we characterized both SP- and MC-modified TNPs in the solid-state by surface-enhanced Raman scattering (SERS) technique and compared the experimental spectra with DFT-calculated Raman spectra (Figure S2). The experimental Raman stretches of closed-ring SP for various vibrations are in agreement with the literature and/or calculated spectra. Importantly, a new C═N stretch and C−N−C scissoring caused by the ring opening of SP to MC appear at 1525 and 715 cm^{-1}, respectively. Additionally, ring opening also causes a loss of the O−C−N stretch at 951 cm^{-1} in the SERS spectrum of MC (see Tables S1 and S2). SP is a closed-ring aromatic structure with low polarity, whereas MC is an open zwitterionic structure with high polarity, which can be verified by conducting a water contact angle measurement. As shown in Figure 2E, 75%:25% mixed SP-UT and UT SAMs has a contact angle of 94.0°, suggesting hydrophobicity. On the other hand, formation of hydroxyl and quaternary ammonium sites (see Figure 1A) by light exposure in the mixed MC-UT and UT SAMs causes a contact angle of 82.3°, which suggests a hydrophilic surface. The trend in water contact angle values for our system is in agreement with the literature where SP-containing molecules were tethered on a glass surface.[30] Taken together, our SERS and water contact angle measurements unequivocally prove that UV light exposure converted SP to MC that results in a λ_{LSPR} red-shift of ∼24 nm.

Achieving reversible photoswitching between SP and MC conformations is a key component in fabricating an adaptable, LSPR-based biosensing device. Reversible conformational changes of such "molecular machines" under repeated light exposure require an appropriate geometric construct on the nanoscale level. Additionally, plasmonic nanostructures and their surface coating, e.g., SAMs, should be stable over a long period of time. Figure 2F represents the λ_{LSPR} upon repeated cycling of our photoswitch-based molecular machine between UV and vis light exposures. Even after five full cycles of SP-MC conformational changes, the nanosystem displays a nearly identical $\Delta\lambda_{LSPR}$ shift of an average 24 nm. This result indicates that our system is stable and can undergo reversible switching without compromising its efficiency. We believe that an appropriate packing of the SAM is the key allowing the reversible photoswitching over several cycles. Moreover, the entire photoisomerization study was conducted in the air, therefore there is a negligible chance for the zwitterion MC form to be involved in a chemical side reaction such as proton capture, which could prevent the transformation of the MC to SP form.[31] Figure 2G shows the LSPR extinction spectra after the first exposure cycle and then after the fifth cycle, where no dramatic change in the λ_{LSPR} value and extinction peak shape are observed. This consistency further suggests that during cycling light exposure, the Au−S bond remains intact. This is because the soft−soft interaction between S and Au provides high chemical stability. Such stability is extremely important for the next stage, which is the design of a plasmonic-based adaptable biosensor with light-controlled receptor binding properties in solution. It has been shown that light exposure to metallic nanoparticles can result in photooxidation and charge accumulation, which influences their LSPR properties.[32,33] To verify that the observed, reversible 24 nm shift of our nanosystem upon exposure to UV and visible light is due to photoreversibility of SP and MC forms and not due to photooxidation and charge accumulation, we exposed TEA-passivated Au TNPs to UV light for 10 min and then collected the extinction spectra. No apparent change in the λ_{LSPR} position and shape of the extinction spectrum are observed (Figure S3). Similarly, visible light exposure does not show any change in the LSPR properties as well. This control experiment indicates that the observed repeatable shifts in the λ_{LSPR} position are solely due to reversible photoisomerization between SP and MC structures.

Photoisomerization between SP and MC of our SP-UT and UT mixed SAM-functionalized Au TNP provides a $\Delta\lambda_{LSPR}$ value of 24 nm. Photoswitching of SP to MC causes an increase in the height of the SAM. On the basis of the extended geometry of SP-UT and MC-UT, we calculated the molecular lengths between the Au atom to the furthest atom in the aromatic ring to be 2.66 and 2.92 nm, respectively (Figure S1B,C). It follows that an average 24 nm λ_{LSPR} shift is quite unprecedented and surprising considering an increase of only 0.26 nm in the thickness of the local dielectric hydrocarbon layer around TNPs. According to the calibration curve we developed (Figure S1A) for $\Delta\lambda_{LSPR}$ as a function of dielectric layer thickness, a 0.26 nm change in the thickness should provide a $\Delta\lambda_{LSPR}$ value of only 5.4 nm. Therefore, we hypothesize that a large portion of observed $\Delta\lambda_{LSPR}$ is caused by dipole−dipole interactions between the zwitterionic MC form and attached TNPs. We calculated the dipole moment of SP-UT and MC-UT molecules to be 2.77 and

https://doi.org/10.1021/acs.analchem.1c02990
Anal. Chem. 2021, 93, 13935−13944

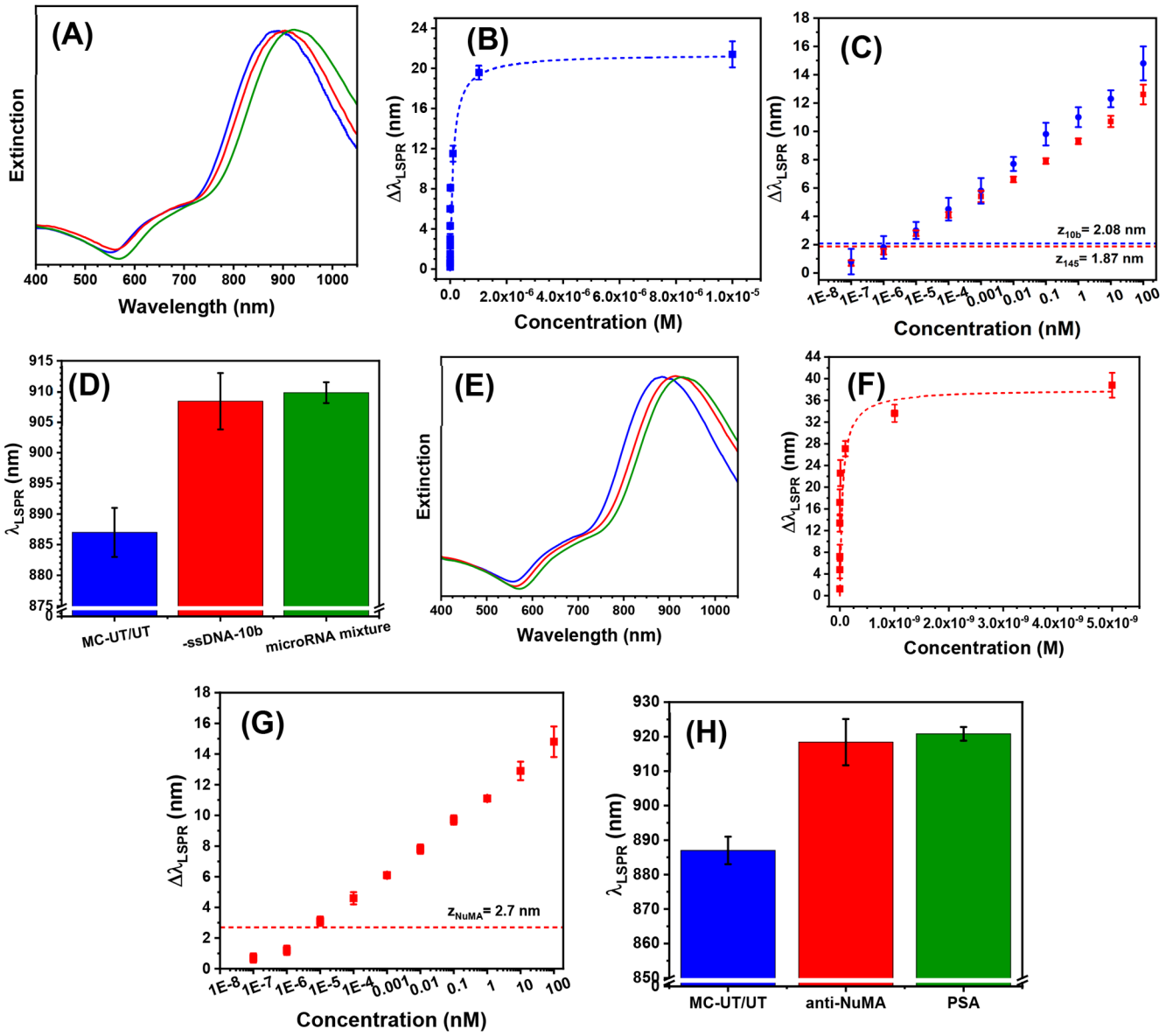

Figure 3. Spectroscopic characterization of the adaptable biosensor. (A) UV−visible extinction spectra of MC-UT:UT SAM-modified TNPs before (blue, λ_{LSPR} = 888.9 nm), after incubation in10 μM -ssDNA-10b in PBS buffer (red, λ_{LSPR} = 910.3 nm), and followed by incubation in 100 nM microRNA-10b in 10% human plasma (green, λ_{LSPR} = 925.1 nm). (B) An adsorption isotherm of -ssDNA-10b on MC-UT:UT SAM-modified surface. (C) Calibration curves of microRNA-10b (blue) and microRNA-145 (red) in human plasma in the range of 100 nM to 100 aM concentrations. (D) Bar graph representation of microRNA-10b specificity test: MC-UT:UT SAM-modified TNPs (blue, λ_{LSPR} = 887.0 nm), incubation in 10 μM -ssDNA-10b (red, λ_{LSPR} = 908.4 nm), and finally incubation in a mixture of 100 nM of each microRNA-145, 143, 490-5p, 96 solution (green, λ_{LSPR} = 909.8 nm). (E) UV−visible extinction spectra of MC-UT:UT SAM-modified TNPs before (blue, λ_{LSPR} = 885.0 nm), after incubation in 100 ng/mL anti-NuMA solution in PBS buffer (red, λ_{LSPR} = 916.4 nm), and finally after incubation in 100 nM NuMA in 10% human urine (green, λ_{LSPR} = 931.2 nm). (F) An adsorption isotherm of anti-NuMA on a MC-UT:UT SAM-modified surface. (G) Calibration curve of 100 nM to 100 aM NuMA in urine (red). (H) The bar graph of NuMA specificity test: MC-UT:UT-SAM modified TNPs (blue, λ_{LSPR} = 887.0 nm), after adsorption of anti-NuMA (red, λ_{LSPR} = 918.4 nm), and then incubation of the biosensor in 100 nM PSA solution in 10% urine (green, λ_{LSPR} = 920.8 nm). After each incubation, biosensors were rinsed with RNase free water, and then extinction spectra were collected. The LOD was derived by using a Z value of the blank (Z = mean + 3σ, σ = standard deviation of blank), which was obtained from six $\Delta\lambda_{LSPR}$ measurements using six different biosensors and substituting the Z value into the "Y" in the calibration curve equation allowing for the LOD concentration ("X") to be obtained.

23.78 D, respectively. This large change in dipole moment to a highly polar MC system can significantly change the local refractive index around TNPs. Therefore, the dipole moment difference between SP and MC could manipulate the plasmonic properties of the nanosystem differently, and the plasmonic TNP and the dipolar organic molecular shell could more strongly couple in the MC form. Additional explanations including mathematical treatment are provided in the Supporting Information.

Equation 1 below shows the relationship between λ_{LSPR} and n.[24,34] Here, λ_{LSPR} and λ_p are the LSPR peak wavelength and bulk plasma frequency of the metal, respectively.

$$\lambda_{LSPR} = \lambda_p(\sqrt{2n^2 + 1}) \quad (1)$$

https://doi.org/10.1021/acs.analchem.1c02990
Anal. Chem. 2021, 93, 13935−13944

Clearly, a change in the dipole moment of the nanostructure surface-bound organic ligand shell can influence the λ_{LSPR}, as observed in our nanosystem between SP and MC. Nevertheless, to the best of our knowledge, this is the first example in which photoisomerization of SP to MC is observed on a nanometer-scale, solid-state device by monitoring the LSPR property. Due to their highest LSPR response, we used 75%:25% mixed SP-UT:UT SAMs for our biosensing application as described below.

Development of an Adaptable Nanoplasmonic Biosensor. As shown in Figure 1, we designed a novel nanoplasmonic biosensor that has the ability for highly sensitive measurement of microRNAs and proteins in an identical biosensor construct by simply exchanging the attached receptor molecules by light exposure. We selected these two types of biomolecules because they are excellent biomarkers for early detection of various cancers in liquid biopsies. Numerous studies have shown that microRNA-10b and -145 and protein NuMA are highly specific biomarkers for bladder cancer from two different biological fluids (plasma and urine).[26,35−39] Figure 3A illustrates the UV−vis extinction spectra of Au TNPs during different functionalization steps in which a receptor (-ssDNA) bound to the zwitterionic MC form (Figure 1c,e) is designated as a microRNA "nanoplasmonic biosensor". Incubation in an aqueous 10 μM -ssDNA-10b solution provides a ∼21 nm λ_{LSPR} red-shift, which is the result of electrostatic adsorption of -ssDNA-10b onto the zwitterionic MC. This shift is mostly from dipole−dipole interactions between -ssDNA-10b and Au TNPs. The change in $\Delta\lambda_{LSPR}$ value is significant considering the molecular weight (MW) of -ssDNA-10b is 7.3 kDa, and it is ∼2.92 nm away from the TNP surface. We also believe that the nucleic acid dipoles in -ssDNA may in some manner interact with the MC dipoles and together influence the λ_{LSPR} as a consequence of dipole−dipole interaction.

To investigate this interaction further, we performed a control experiment by incubating the same MC-UT modified sensor in a 10 μM aqueous solution of sodium poly(acrylate) (PAA, MW = 15 kDa). The negatively charged oxygen pendant group in the polymer backbone mimics the−ssDNA charge but the bases are lacking. We observe a $\Delta\lambda_{LSPR}$ of ∼5 nm (Figure S4), which is in agreement with the loss of a dipole effect. It is important to mention that the charge−charge interaction between -ssDNAs and zwitterionic MC forms is a thermodynamically driven process. Therefore, one would expect that such interactions should be strong and instantaneous. As illustrated in Figure 3B, we observe a strong binding affinity between the zwitterionic MC surface and -ssDNA-10b with an equilibrium binding dissociation constant (K_d) of 106 nM, as determined from the Langmuir isotherm.[40] Additionally, it is important to determine the time required to obtain a fully -ssDNA covered MC surface since a shorter incubation time (<120 min) could potentially reduce the overall assay time for practical application of our biosensors. We are actively investigating the kinetic aspect of this interaction, and our findings will be reported in a future publication.

In a separate control experiment, incubation of 75%:25% mixed SAM of SP-UT and UT modified TNPs in a PBS buffer solution of 10 μM -ssDNA-10b does not provide any detectable λ_{LSPR} shift (Figure S5), suggesting -ssDNAs only adsorbs onto the charged MC surface due to electrostatic interaction and not on the neutral SP surface. Finally, incubation of the nanoplasmonic biosensor designed for microRNA-10b detection displays an additional 15 nm λ_{LSPR} red-shift (Figure 3A). Extinction spectra relevant to microRNA-145 detection are provided in the Supporting Information (Figure S6). The limits of detection (LODs) for microRNA-10b and -145 are 1.87 and 1.50 femtomolar (fM), respectively, in human plasma (Figure 3C). The LODs for these microRNAs are in the attomolar (aM) range in PBS buffer (without human plasma; Figure S7 and Table S3). These LODs for the detection of microRNAs and proteins are comparable to TNP-based nonadaptable biosensors that we reported previously; suggesting the performance of adaptable biosensors is comparable to a single biosensor type where only microRNAs or proteins can be detected and not both.[29,41]

Specificity and Adaptability Tests of Nanoplasmonic Biosensors. Although LSPR sensitivity can be enhanced by selecting larger aspect ratio nanostructures that display an λ_{LSPR} at longer wavelengths (>800 nm), the plasmonic line-width increases with an increasing aspect ratio, therefore broadening the LSPR peak and increasing nonspecificity in biosensing.[34,42] Herein, we have shown that functionalizing Au TNPs with appropriate SAMs bearing zwitterion molecules can shift the λ_{LSPR} to longer wavelengths (enhancing sensing efficiency) without physically changing the aspect ratio of a nanostructure. We also examined the specificity of our nanoplasmonic biosensor because it is critically important in clinical diagnostics. This is more important in the current construct, since all the interactions are electrostatic and any plasma microRNAs can adsorb on unoccupied MC sites providing a false response. The nanoplasmonic biosensor designed to detect microRNA-10b was incubated in a 10% plasma solution containing microRNA-145, -143, -490-5p, and -96 (10.0 nM/microRNA), which are found to be over and/or underexpressed in bladder cancer, and after washing the biosensor and measuring the extinction spectrum, provides $\Delta\lambda_{LSPR}$ ∼ 1.4 nm (Figure 3D). This shift could be due to transient adsorption of some microRNAs and/or instrumental noise.

The specificity of our biosensor is further illustrated by detecting and quantifying NuMA protein, which is an approved biomarker for bladder cancer. Incubation of 75%:25% mixed MC-UT and UT SAM-functionalized Au TNPs in a 100 ng/mL of anti-NuMA solution provides a $\Delta\lambda_{LSPR}$ of 32 nm (Figure 3E). Then after rinsing the biosensor followed by incubation in 100 nM NuMA in 10% urine there is an additional 15 nm red-shift. We determined that the interaction between anti-NuMA and the zwitterion MC surface is strong with a K_d of 5.05 pM (Figure 3F). The LODs for NuMA in 10% urine and PBS buffer are 5.0 fM and 130 aM, respectively (Figures 3G and S8 and Table S4). Finally, we tested the biosensor specificity for protein detection by incubating it in a 100 nM prostate specific antigen (PSA) solution, and a negligible $\Delta\lambda_{LSPR}$ of 1.1 nm is observed (Figure 3H). This result is significant and suggests that although our biosensing mechanism relies on the charge−charge interaction between MC-receptor and receptor-analyte molecules, under our optimized fabrication strategy, nonspecific adsorption of unwanted biomolecules, and thus false positive responses, are avoided.

We further demonstrate the regenerative testing capabilities for different biomarkers (adaptability), e.g., first as a microRNA assay and then regenerating the biosensor to measure proteins, all using the same device and identical signal output. Our strategy is less labor intensive than PCR and ELISA, offers very good protocol verification, and provides excellent biosensor calibration and standardization. As schematically illustrated in Figure 4A, the NuMA biosensor was prepared, and its λ_{LSPR}

https://doi.org/10.1021/acs.analchem.1c02990
Anal. Chem. 2021, 93, 13935−13944

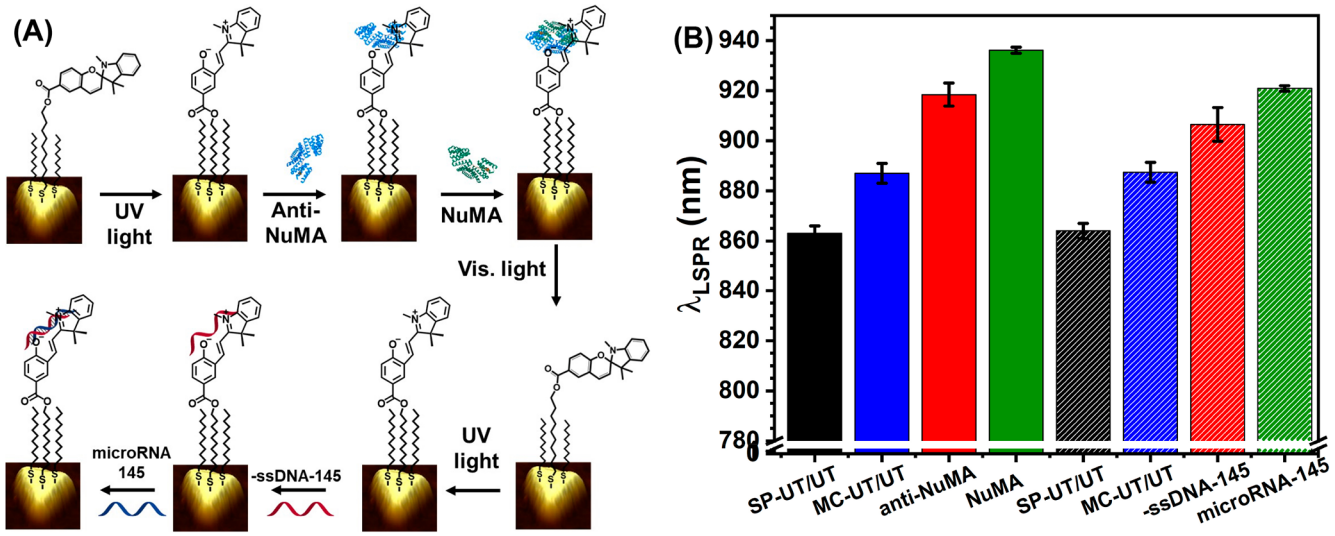

Figure 4. Demonstration of biosensor's adaptability. (A) Schematic diagram representing adaptability of the nanoplasmonic biosensor to detect both microRNA-10b and NuMA protein. (B) Bar graph representation of adaptability of the biosensor to detect both microRNA-145 and NuMA protein: SP-UT/UT (black, λ_{LSPR} = 863.0 nm), MC-UT/UT (blue, λ_{LSPR} = 887.4 nm), anti-NuMA (red, λ_{LSPR} = 918.8 nm), 100 nM NuMA (green, λ_{LSPR} = 936.1 nm), SP-UT/UT (black dashed, λ_{LSPR} = 864.2 nm), MC-UT/UT (blue dashed, λ_{LSPR} = 887.4 nm), -ssDNA-145 (red dashed, λ_{LSPR} = 906.5 nm), and 100 nM microRNA-145 (green dashed, λ_{LSPR} = 920.9 nm). After each incubation, biosensors were rinsed with RNase free water, and then extinction spectra were collected.

value was determined in 100 nM NuMA, yielding a $\Delta\lambda_{LSPR}$ of 16.7 nm (Figure 4B). The biosensor was then rinsed with 2.5 M PBS buffer to weaken the protein−protein and protein−MC interactions through charge screening, rinsed in water, dried under a N_2 flow, and finally exposed to visible light for 10 min converting MC to SP and regenerating the original SP conformation on the Au TNPs, which display an λ_{LSPR} at 864 nm implying removal of the bound receptor/analyte pairs. This value is within the range of freshly prepared, 75%:25% mixed SP-UT and UT SAM-functionalized Au TNPs (Figure 2C). Next, we exposed this substrate to UV light to generate the activated MC form, which was incubated in 10 μM -ssDNA-145 as the new receptor. After washing, the biosensor was incubated with 100 nM microRNA-145 in 10% human plasma. The biosensor sensitivity after regeneration and assaying microRNA-145 in plasma following the initial detection of NuMA protein in urine is comparable to freshly prepared biosensors with a 99.7% recovery. Although the interaction between the zwitterion MC form and receptor molecules (either -ssDNA-10*b*/145 or anti-NuMA) are relatively strong, the activation energy for SP-MC isomerization is ∼50 kJ/mol in polar solvents.[43,44] We believe washing the biosensors with a high concentration of electrolyte solution and this relatively low activation energy allow the biosensors to regenerate to the nonreceptor binding SP motif.

Clinical Sample Analysis Utilizing Adaptable Nanoplasmonic Biosensors. To evaluate the performance of our adaptable nanoplasmonic biosensor assay strategy for diagnosis of clinical samples, 10 metastatic (MT) bladder cancer patients plasma were analyzed to detect and quantify both microRNA-10b and microRNA-145. MicroRNA-10b and microRNA-145 are oncogenic and tumor-suppressor biomolecules, respectively, and the microRNA-10b level increases whereas the microRNA-145 level decreases in cancer patient versus healthy subjects (normal control, NC). As shown in Figure 5A,B, both microRNAs are highly selective biomarkers to distinguish cancer patients (n = 10) from NC (n = 10) with p values ranging 0.0002 to 0.0001. We also quantified NuMA protein for the above cancer patients by analyzing urine samples (p < 0.0001) (Figure 5C). Receiving operating characteristic analysis reveals that the biosensor is highly specific and can discriminate between the NC versus the disease group with an area under the curve of 1.0 (Figure 5D). Importantly, to the best of our knowledge, this is the first example where both nucleic acid and protein biomarkers are assayed utilizing a single instrument and under identical sensing mechanism, reducing time-lag dramatically, and improving diagnosis by faster data correlation. As schematically represented in Figure 5E, we detected and quantified microRNA-10b from a patient plasma and regenerated the biosensor MC motif, which was then used to analyze a standard of 100 nM microRNA-10b. The LSPR data presented in Figure 5F show that even after patient sample analysis, our nanoplasmonic biosenors can be regenerated and to detect microRNAs with a similar efficiency as freshly prepared biosensors. This approach can be used for protocol verification to confirm that our sensor operates with 100% efficiency.

■ CONCLUSION

In conclusion, by utilizing the highly polar form of a photoisomerizable molecular switch, i.e., SP to-MC, chemically attached onto Au TNPs via SAMs, we have demonstrated that the LSPR response can be modulated by nonradiative dipole−dipole interactions without changing the physical dimensions of the nanostructures and surrounding dielectric components. Moreover, using the extraordinary range of structure and properties of the SP-based system, we have constructed a responsive nanosystem, which has now been used for an ultrasensitive assay of both nucleic acids and proteins adaptively with identical workflow and highly selective device readout. As a proof-of-concept, we have also shown that our sensing approach can be applied to detect bladder cancer biomarkers from different human biofluids. Taken together, we believe that our newly developed, label-free, optical-based technology can be used for rapid clinical setting detection of other cancers, thus it may provide a new paradigm in early detection of several

https://doi.org/10.1021/acs.analchem.1c02990
Anal. Chem. 2021, 93, 13935−13944

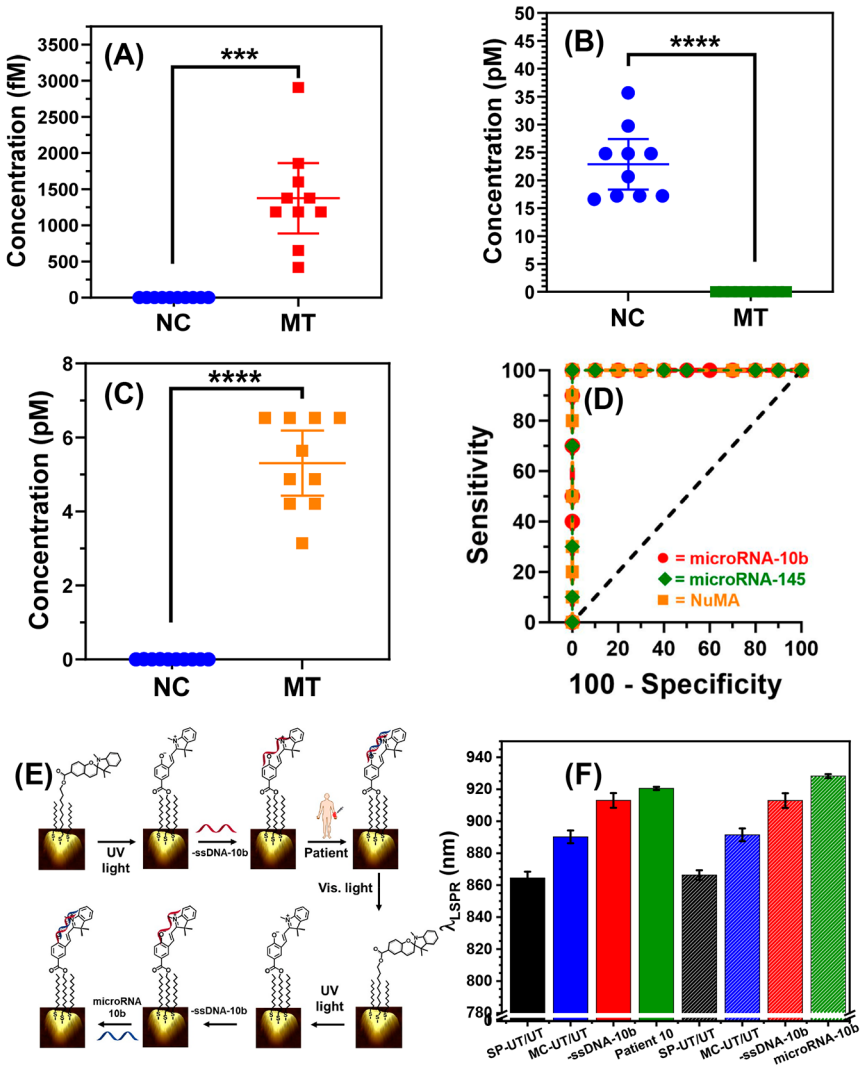

Figure 5. Analysis of clinical samples using adaptable biosensors. Quantification of (A) microRNA-10b, (B) microRNA-145, and (C) NuMA in 10 bladder cancer patient plasma samples (metastatic, MT) and 10 healthy plasma samples (normal control, NC). The p values were determined by paired t test: ***$p < 0.0002$ and ****$p < 0.0001$. (D) Receiving operative characteristic curve of microRNA-10b, microRNA-145, and NuMA of MT bladder cancer patients and NC samples. (E) Schematic representation of protocol verification in which microRNA-10b was quantified using the biosensor, the biosensor was regenerated, and then the proficiency was measured using a known concentration of microRNA-10b. (F) Bar graph representation of the confirmation test: mixed SP-UT and UT (black, $\lambda_{LSPR} = 864.4$ nm), MC-UT and UT (blue, $\lambda_{LSPR} = 890.2$ nm), -ssDNA-10b (red, $\lambda_{LSPR} = 913.0$ nm), patient sample MT-10 microRNA-10b quantification (green, $\lambda_{LSPR} = 920.5$ nm), mixed SP-UT and UT (dashed black, $\lambda_{LSPR} = 866.3$ nm), MC-UT and UT (dashed blue, $\lambda_{LSPR} = 891.5$ nm), -ssDNA-10b (dashed red, $\lambda_{LSPR} = 912.9$ nm), and 100 nM microRNA-10b (dashed green, $\lambda_{LSPR} = 928.2$ nm).

biomarkers from different biofluids for noninvasive *"liquid biopsies."*

■ ASSOCIATED CONTENT

Supporting Information

The Supporting Information is available free of charge at https://pubs.acs.org/doi/10.1021/acs.analchem.1c02990.

Detailed experimental procedure of HS-C11-SP and TNP syntheses, surface modification, UV−visible extinction spectra, Raman spectra, and Tables for different calibration data (PDF)

■ AUTHOR INFORMATION

Corresponding Author

Rajesh Sardar − *Department of Chemistry and Chemical Biology, Indiana University−Purdue University Indianapolis, Indianapolis, Indiana 46202, United States; Integrated Nanosystems Development Institute, Indiana University−Purdue University Indianapolis, Indianapolis, Indiana 46202, United States;* orcid.org/0000-0001-9680-1301; Email: rsardar@iupui.edu

Authors

Sumon Hati − *Department of Chemistry and Chemical Biology, Indiana University−Purdue University Indianapolis, Indianapolis, Indiana 46202, United States;* orcid.org/0000-0002-4165-8314

https://doi.org/10.1021/acs.analchem.1c02990
Anal. Chem. 2021, 93, 13935−13944

Sarah R. Langlais − *Department of Chemistry and Chemical Biology, Indiana University−Purdue University Indianapolis, Indianapolis, Indiana 46202, United States*
Adrianna N. Masterson − *Department of Chemistry and Chemical Biology, Indiana University−Purdue University Indianapolis, Indianapolis, Indiana 46202, United States*
Thakshila Liyanage − *Department of Chemistry and Chemical Biology, Indiana University−Purdue University Indianapolis, Indianapolis, Indiana 46202, United States;* Present Address: Old Dominion University, Norfolk, VA, 23539
Barry B. Muhoberac − *Department of Chemistry and Chemical Biology, Indiana University−Purdue University Indianapolis, Indianapolis, Indiana 46202, United States*
Hristos Kaimakliotis − *Department of Urology, Indiana University School of Medicine, Indianapolis, Indiana 46202, United States*
Merrell Johnson − *Department of Physics, Purdue University Fort Wayne, Fort Wayne, Indiana 46805, United States*

Complete contact information is available at: https://pubs.acs.org/10.1021/acs.analchem.1c02990

Author Contributions

⊥Contributed equally to this work.

Notes

The authors declare no competing financial interest.

■ ACKNOWLEDGMENTS

This work was partially supported by funding from the National Science Foundation (CBET-1604617) and IUPUI Bridge funding. The authors also thank Indiana University Simon Cancer Center for collecting plasma and urine specimens from bladder cancer patients for this study.

■ REFERENCES

(1) Balzani, V.; Gomez-Lopez, M.; Stoddart, J. F. *Acc. Chem. Res.* **1998**, *31*, 405−414.
(2) Weiss, P. S. *Acc. Chem. Res.* **2008**, *41*, 1772−1781.
(3) Klajn, R.; Wesson, P. J.; Bishop, K. J. M.; Grzybowski, B. A. *Angew. Chem., Int. Ed.* **2009**, *48*, 7035−7039.
(4) Klajn, R.; Stoddart, J. F.; Grzybowski, B. A. *Chem. Soc. Rev.* **2010**, *39*, 2203−2237.
(5) Robertus, J.; Browne, W. R.; Feringa, B. L. *Chem. Soc. Rev.* **2010**, *39*, 354−378.
(6) Yan, Y.; Chen, J. I. L.; Ginger, D. S. *Nano Lett.* **2012**, *12*, 2530−2536.
(7) Green, J. E.; Wook Choi, J.; Boukai, A.; Bunimovich, Y.; Johnston-Halperin, E.; DeIonno, E.; Luo, Y.; Sheriff, B. A.; Xu, K.; Shik Shin, Y.; Tseng, H.-R.; Stoddart, J. F.; Heath, J. R. *Nature* **2007**, *445*, 414−417.
(8) Brouwer, A. M.; Frochot, C. l.; Gatti, F. G.; Leigh, D. A.; Mottier, L. Ã.; Paolucci, F.; Roffia, S.; Wurpel, G. W. H. *Science (Washington, DC, U. S.)* **2001**, *291*, 2124−2128.
(9) Donhauser, Z. J.; Mantooth, B. A.; Kelly, K. F.; Bumm, L. A.; Monnell, J. D.; Stapleton, J. J.; Price, D. W.; Rawlett, A. M.; Allara, D. L.; Tour, J. M.; Weiss, P. S. *Science (Washington, DC, U. S.)* **2001**, *292*, 2303−2307.
(10) Li, M.; Zhao, J.; Chu, H.; Mi, Y.; Zhou, Z.; Di, Z.; Zhao, M.; Li, L. *Adv. Mater.* **2019**, *31*, 1804745.
(11) Klajn, R. *Chem. Soc. Rev.* **2014**, *43*, 148−184.
(12) Kortekaas, L.; Browne, W. R. *Chem. Soc. Rev.* **2019**, *48*, 3406−3424.
(13) Zhu, L.; Zhu, M.-Q.; Hurst, J. K.; Li, A. D. Q. *J. Am. Chem. Soc.* **2005**, *127*, 8968−8970.
(14) Di Benedetto, F.; Mele, E.; Camposeo, A.; Athanassiou, A.; Cingolani, R.; Pisignano, D. *Adv. Mater.* **2008**, *20*, 314−318.
(15) Rosario, R.; Gust, D.; Hayes, M.; Springer, J.; Garcia, A. A. *Langmuir* **2003**, *19*, 8801−8806.
(16) Bunker, B. C.; Kim, B. I.; Houston, J. E.; Rosario, R.; Garcia, A. A.; Hayes, M.; Gust, D.; Picraux, S. T. *Nano Lett.* **2003**, *3*, 1723−1727.
(17) Blonder, R.; Levi, S.; Tao, G.; Ben-Dov, I.; Willner, I. *J. Am. Chem. Soc.* **1997**, *119*, 10467−10478.
(18) Joshi, G. K.; Blodgett, K. N.; Muhoberac, B. B.; Johnson, M. A.; Smith, K. A.; Sardar, R. *Nano Lett.* **2014**, *14*, 532−540.
(19) Kumar, A. S.; Ye, T.; Takami, T.; Yu, B.-C.; Flatt, A. K.; Tour, J. M.; Weiss, P. S. *Nano Lett.* **2008**, *8*, 1644−1648.
(20) Zheng, Y. B.; Yang, Y.-W.; Jensen, L.; Fang, L.; Juluri, B. K.; Flood, A. H.; Weiss, P. S.; Stoddart, J. F.; Huang, T. J. *Nano Lett.* **2009**, *9*, 819−825.
(21) Halas, N. J.; Lal, S.; Chang, W.-S.; Link, S.; Nordlander, P. *Chem. Rev.* **2011**, *111*, 3913−3961.
(22) Duan, H.; Fernández-Domínguez, A. I.; Bosman, M.; Maier, S. A.; Yang, J. K. W. *Nano Lett.* **2012**, *12*, 1683−1689.
(23) El-Sayed, M. A. *Acc. Chem. Res.* **2001**, *34*, 257−264.
(24) Zhao, J.; Pinchuk, A. O.; McMahon, J. M.; Li, S.; Ausman, L. K.; Atkinson, A. L.; Schatz, G. C. *Acc. Chem. Res.* **2008**, *41*, 1710−1720.
(25) Joshi, G. K.; Deitz-McElyea, S.; Liyanage, T.; Lawrence, K.; Mali, S.; Sardar, R.; Korc, M. *ACS Nano* **2015**, *9*, 11075−11089.
(26) Liyanage, T.; Masterson, A. N.; Oyem, H. H.; Kaimakliotis, H.; Nguyen, H.; Sardar, R. *Anal. Chem.* **2019**, *91*, 1894−1903.
(27) Masterson, A. N.; Liyanage, T.; Kaimakliotis, H.; Gholami Derami, H.; Deiss, F.; Sardar, R. *Anal. Chem.* **2020**, *92*, 9295−9304.
(28) Haes, A. J.; Van Duyne, R. P. *J. Am. Chem. Soc.* **2002**, *124*, 10596−10604.
(29) Joshi, G. K.; Deitz-McElyea, S.; Johnson, M.; Mali, S.; Korc, M.; Sardar, R. *Nano Lett.* **2014**, *14*, 6955−6963.
(30) Rosario, R.; Gust, D.; Hayes, M.; Jahnke, F.; Springer, J.; Garcia, A. A. *Langmuir* **2002**, *18*, 8062−8069.
(31) Kundu, P. K.; Samanta, D.; Leizrowice, R.; Margulis, B.; Zhao, H.; Börner, M.; Udayabhaskararao, T.; Manna, D.; Klajn, R. *Nat. Chem.* **2015**, *7*, 646−652.
(32) Redmond, P. L.; Wu, X.; Brus, L. *J. Phys. Chem. C* **2007**, *111*, 8942−8947.
(33) Wu, X.; Thrall, E. S.; Liu, H.; Steigerwald, M.; Brus, L. *J. Phys. Chem. C* **2010**, *114*, 12896−12899.
(34) Mayer, K. M.; Hafner, J. H. *Chem. Rev.* **2011**, *111*, 3828−3857.
(35) De Long, J.; Sullivan, T. B.; Humphrey, J.; Logvinenko, T.; Summerhayes, K. A.; Kozinn, S.; Harty, N.; Summerhayes, I. C.; Libertino, J. A.; Holway, A. H.; Rieger-Christ, K. M. *Am. J. Transl. Res.* **2015**, *7*, 2500−2518.
(36) D'Costa, J. J.; Goldsmith, J. C.; Wilson, J. S.; Bryan, R. T.; Ward, D. G. *Bladder Cancer* **2016**, *2*, 301−317.
(37) Proctor, I.; Stoeber, K.; Williams, G. H *Histopathology* **2010**, *57*, 1−13.
(38) James, N. D.; Hussain, S. A.; Hall, E.; Jenkins, P.; Tremlett, J.; Rawlings, C.; Crundwell, M.; Sizer, B.; Sreenivasan, T.; Hendron, C.; Lewis, R.; Waters, R.; Huddart, R. A. *N. Engl. J. Med.* **2012**, *366*, 1477−1488.
(39) Xiao, H.; Li, H.; Yu, G.; Xiao, W.; Hu, J.; Zeng, K. T. J.; He, W.; Zeng, G.; Ye, Z.; Xu, H.; Tang, H. *Oncol. Rep.* **2014**, *31*, 1832−1838.
(40) Shi, B.; Shin, Y. K.; Hassanali, A. A.; Singer, S. J. *J. Phys. Chem. B* **2015**, *119*, 11030−11040.
(41) Liyanage, T.; Sangha, A.; Sardar, R. *Analyst* **2017**, *142*, 2442−2450.
(42) Nusz, G. J.; Curry, A. C.; Marinakos, S. M.; Wax, A.; Chilkoti, A. *ACS Nano* **2009**, *3*, 795−806.
(43) Wohl, C. J.; Kuciauskas, D. *J. Phys. Chem. B* **2005**, *109*, 22186−22191.
(44) Zhang, S.; Zhang, Q.; Ye, B.; Li, X.; Zhang, X.; Deng, Y. *J. Phys. Chem. B* **2009**, *113*, 6012−6019.